Resolving the Extragalactic γ-Ray Background above 50 GeV with the Fermi Large Area Telescope

M. Ackermann,[1] M. Ajello,[2,*] A. Albert,[3] W. B. Atwood,[4] L. Baldini,[5,3] J. Ballet,[6] G. Barbiellini,[7,8] D. Bastieri,[9,10] K. Bechtol,[11] R. Bellazzini,[12] E. Bissaldi,[13] R. D. Blandford,[3] E. D. Bloom,[3] R. Bonino,[14,15] J. Bregeon,[16] R. J. Britto,[17] P. Bruel,[18] R. Buehler,[1] G. A. Caliandro,[3,19] R. A. Cameron,[3] M. Caragiulo,[20,13] P. A. Caraveo,[21] E. Cavazzuti,[22] C. Cecchi,[23,24] E. Charles,[3] A. Chekhtman,[25] J. Chiang,[3] G. Chiaro,[10] S. Ciprini,[22,23] J. Cohen-Tanugi,[16] L. R. Cominsky,[26] F. Costanza,[13] S. Cutini,[22,27,23] F. D'Ammando,[28,29] A. de Angelis,[30] F. de Palma,[13,31] R. Desiante,[32,14] S. W. Digel,[3] M. Di Mauro,[3,†] L. Di Venere,[20,13] A. Domínguez,[2] P. S. Drell,[3] C. Favuzzi,[20,13] S. J. Fegan,[18] E. C. Ferrara,[33] A. Franckowiak,[3] Y. Fukazawa,[34] S. Funk,[35] P. Fusco,[20,13] F. Gargano,[13] D. Gasparrini,[22,23] N. Giglietto,[20,13] P. Giommi,[22] F. Giordano,[20,13] M. Giroletti,[28] G. Godfrey,[3] D. Green,[36,33] I. A. Grenier,[6] S. Guiriec,[33,37] E. Hays,[33] D. Horan,[18] G. Iafrate,[7,38] T. Jogler,[3] G. Jóhannesson,[39] M. Kuss,[12] G. La Mura,[10,40] S. Larsson,[41,42] L. Latronico,[14] J. Li,[43] L. Li,[41,42] F. Longo,[7,8] F. Loparco,[20,13] B. Lott,[44] M. N. Lovellette,[45] P. Lubrano,[23,24] G. M. Madejski,[3] J. Magill,[36] S. Maldera,[14] A. Manfreda,[12] M. Mayer,[1] M. N. Mazziotta,[13] P. F. Michelson,[3] W. Mitthumsiri,[46] T. Mizuno,[47] A. A. Moiseev,[48,36] M. E. Monzani,[3] A. Morselli,[49] I. V. Moskalenko,[3] S. Murgia,[50] M. Negro,[14,15] E. Nuss,[16] T. Ohsugi,[47] C. Okada,[34] N. Omodei,[3] E. Orlando,[3] J. F. Ormes,[51] D. Paneque,[52,3] J. S. Perkins,[33] M. Pesce-Rollins,[12,3] V. Petrosian,[3] F. Piron,[16] G. Pivato,[12] T. A. Porter,[3] S. Rainò,[20,13] R. Rando,[9,10] M. Razzano,[12,53] S. Razzaque,[17] A. Reimer,[40,3] O. Reimer,[40,3] T. Reposeur,[44] R. W. Romani,[3] M. Sánchez-Conde,[42,54] J. Schmid,[6] A. Schulz,[1] C. Sgrò,[12] D. Simone,[13] E. J. Siskind,[55] F. Spada,[12] G. Spandre,[12] P. Spinelli,[20,13] D. J. Suson,[56] H. Takahashi,[34] J. B. Thayer,[3] L. Tibaldo,[57] D. F. Torres,[43,58] E. Troja,[33,36] G. Vianello,[3] M. Yassine,[16] and S. Zimmer[54,42]

[1]*Deutsches Elektronen Synchrotron DESY, D-15738 Zeuthen, Germany*
[2]*Department of Physics and Astronomy, Clemson University, Kinard Lab of Physics, Clemson, SC 29634-0978, USA*
[3]*W. W. Hansen Experimental Physics Laboratory, Kavli Institute for Particle Astrophysics and Cosmology, Department of Physics and SLAC National Accelerator Laboratory, Stanford University, Stanford, CA 94305, USA*
[4]*Santa Cruz Institute for Particle Physics, Department of Physics and Department of Astronomy and Astrophysics, University of California at Santa Cruz, Santa Cruz, CA 95064, USA*
[5]*Università di Pisa and Istituto Nazionale di Fisica Nucleare, Sezione di Pisa I-56127 Pisa, Italy*
[6]*Laboratoire AIM, CEA-IRFU/CNRS/Université Paris Diderot, Service d'Astrophysique, CEA Saclay, F-91191 Gif sur Yvette, France*
[7]*Istituto Nazionale di Fisica Nucleare, Sezione di Trieste, I-34127 Trieste, Italy*
[8]*Dipartimento di Fisica, Università di Trieste, I-34127 Trieste, Italy*
[9]*Istituto Nazionale di Fisica Nucleare, Sezione di Padova, I-35131 Padova, Italy*
[10]*Dipartimento di Fisica e Astronomia "G. Galilei", Università di Padova, I-35131 Padova, Italy*
[11]*Dept. of Physics and Wisconsin IceCube Particle Astrophysics Center, University of Wisconsin, Madison, WI 53706, USA*
[12]*Istituto Nazionale di Fisica Nucleare, Sezione di Pisa, I-56127 Pisa, Italy*
[13]*Istituto Nazionale di Fisica Nucleare, Sezione di Bari, I-70126 Bari, Italy*
[14]*Istituto Nazionale di Fisica Nucleare, Sezione di Torino, I-10125 Torino, Italy*
[15]*Dipartimento di Fisica Generale "Amadeo Avogadro", Università degli Studi di Torino, I-10125 Torino, Italy*
[16]*Laboratoire Univers et Particules de Montpellier, Université Montpellier, CNRS/IN2P3, Montpellier, France*
[17]*Department of Physics, University of Johannesburg, PO Box 524, Auckland Park 2006, South Africa*
[18]*Laboratoire Leprince-Ringuet, École polytechnique, CNRS/IN2P3, Palaiseau, France*
[19]*Consorzio Interuniversitario per la Fisica Spaziale (CIFS), I-10133 Torino, Italy*
[20]*Dipartimento di Fisica "M. Merlin" dell'Università e del Politecnico di Bari, I-70126 Bari, Italy*
[21]*INAF-Istituto di Astrofisica Spaziale e Fisica Cosmica, I-20133 Milano, Italy*
[22]*Agenzia Spaziale Italiana (ASI) Science Data Center, I-00133 Roma, Italy*
[23]*Istituto Nazionale di Fisica Nucleare, Sezione di Perugia, I-06123 Perugia, Italy*
[24]*Dipartimento di Fisica, Università degli Studi di Perugia, I-06123 Perugia, Italy*
[25]*College of Science, George Mason University, Fairfax, VA 22030, resident at Naval Research Laboratory, Washington, DC 20375, USA*
[26]*Department of Physics and Astronomy, Sonoma State University, Rohnert Park, CA 94928-3609, USA*
[27]*INAF Osservatorio Astronomico di Roma, I-00040 Monte Porzio Catone (Roma), Italy*
[28]*INAF Istituto di Radioastronomia, I-40129 Bologna, Italy*
[29]*Dipartimento di Astronomia, Università di Bologna, I-40127 Bologna, Italy*
[30]*Dipartimento di Fisica, Università di Udine and Istituto Nazionale di Fisica Nucleare, Sezione di Trieste, Gruppo Collegato di Udine, I-33100 Udine*
[31]*Università Telematica Pegaso, Piazza Trieste e Trento, 48, I-80132 Napoli, Italy*
[32]*Università di Udine, I-33100 Udine, Italy*

[33]NASA Goddard Space Flight Center, Greenbelt, MD 20771, USA
[34]Department of Physical Sciences, Hiroshima University, Higashi-Hiroshima, Hiroshima 739-8526, Japan
[35]Erlangen Centre for Astroparticle Physics, D-91058 Erlangen, Germany
[36]Department of Physics and Department of Astronomy, University of Maryland, College Park, MD 20742, USA
[37]NASA Postdoctoral Program Fellow, USA
[38]Osservatorio Astronomico di Trieste, Istituto Nazionale di Astrofisica, I-34143 Trieste, Italy
[39]Science Institute, University of Iceland, IS-107 Reykjavik, Iceland
[40]Institut für Astro- und Teilchenphysik and Institut für Theoretische Physik, Leopold-Franzens-Universität Innsbruck, A-6020 Innsbruck, Austria
[41]Department of Physics, KTH Royal Institute of Technology, AlbaNova, SE-106 91 Stockholm, Sweden
[42]The Oskar Klein Centre for Cosmoparticle Physics, AlbaNova, SE-106 91 Stockholm, Sweden
[43]Institute of Space Sciences (IEEC-CSIC), Campus UAB, E-08193 Barcelona, Spain
[44]Centre d'Études Nucléaires de Bordeaux Gradignan, IN2P3/CNRS, Université Bordeaux 1, BP120, F-33175 Gradignan Cedex, France
[45]Space Science Division, Naval Research Laboratory, Washington, DC 20375-5352, USA
[46]Department of Physics, Faculty of Science, Mahidol University, Bangkok 10400, Thailand
[47]Hiroshima Astrophysical Science Center, Hiroshima University, Higashi-Hiroshima, Hiroshima 739-8526, Japan
[48]Center for Research and Exploration in Space Science and Technology (CRESST) and NASA Goddard Space Flight Center, Greenbelt, Maryland 20771, USA
[49]Istituto Nazionale di Fisica Nucleare, Sezione di Roma "Tor Vergata", I-00133 Roma, Italy
[50]Center for Cosmology, Physics and Astronomy Department, University of California, Irvine, California 92697-2575, USA
[51]Department of Physics and Astronomy, University of Denver, Denver, Colorado 80208, USA
[52]Max-Planck-Institut für Physik, D-80805 München, Germany
[53]Funded by contract FIRB-2012-RBFR12PM1F from the Italian Ministry of Education, University and Research (MIUR)
[54]Department of Physics, Stockholm University, AlbaNova, SE-106 91 Stockholm, Sweden
[55]NYCB Real-Time Computing Inc., Lattingtown, New York 11560-1025, USA
[56]Department of Chemistry and Physics, Purdue University Calumet, Hammond, Indiana 46323-2094, USA
[57]Max-Planck-Institut für Kernphysik, D-69029 Heidelberg, Germany
[58]Institució Catalana de Recerca i Estudis Avançats (ICREA), Barcelona, Spain

(Received 24 October 2015; revised manuscript received 22 February 2016; published 14 April 2016)

The Fermi Large Area Telescope (LAT) Collaboration has recently released a catalog of 360 sources detected above 50 GeV (2FHL). This catalog was obtained using 80 months of data re-processed with Pass 8, the newest event-level analysis, which significantly improves the acceptance and angular resolution of the instrument. Most of the 2FHL sources at high Galactic latitude are blazars. Using detailed Monte Carlo simulations, we measure, for the first time, the source count distribution, dN/dS, of extragalactic γ-ray sources at $E > 50$ GeV and find that it is compatible with a Euclidean distribution down to the lowest measured source flux in the 2FHL ($\sim 8 \times 10^{-12}$ ph cm^{-2} s^{-1}). We employ a one-point photon fluctuation analysis to constrain the behavior of dN/dS below the source detection threshold. Overall, the source count distribution is constrained over three decades in flux and found compatible with a broken power law with a break flux, S_b, in the range $[8 \times 10^{-12}, 1.5 \times 10^{-11}]$ ph cm^{-2} s^{-1} and power-law indices below and above the break of $\alpha_2 \in [1.60, 1.75]$ and $\alpha_1 = 2.49 \pm 0.12$, respectively. Integration of dN/dS shows that point sources account for at least $86^{+16}_{-14}\%$ of the total extragalactic γ-ray background. The simple form of the derived source count distribution is consistent with a single population (i.e., blazars) dominating the source counts to the minimum flux explored by this analysis. We estimate the density of sources detectable in blind surveys that will be performed in the coming years by the Cherenkov Telescope Array.

DOI: 10.1103/PhysRevLett.116.151105

The origin of the extragalactic γ-ray background (EGB), the Universe's glow in γ rays, has been debated since the first measurement with the SAS-2 satellite [1]. The EGB spectrum has been accurately measured, from 100 MeV to 820 GeV, by the Large Area Telescope (LAT) on board the Fermi Gamma-Ray Space Telescope mission [2]. Part of the EGB arises from the emission of resolved and unresolved point sources like blazars, star-forming, and radio galaxies Refs. [e.g. [3–5]], which are routinely detected in γ rays. A possible contribution to the EGB may also come from diffuse processes such as annihilation or decaying dark matter particles (see Ref. [6] for a review).

Here we show for the first time that Fermi LAT is able to resolve the high-energy EGB into pointlike sources. Indeed, thanks to the accrual of 80 months of data (see right panel of Fig. 1) and the increased acceptance and improved point-spread function delivered by the new event-level analysis dubbed Pass 8 [7], the LAT has recently

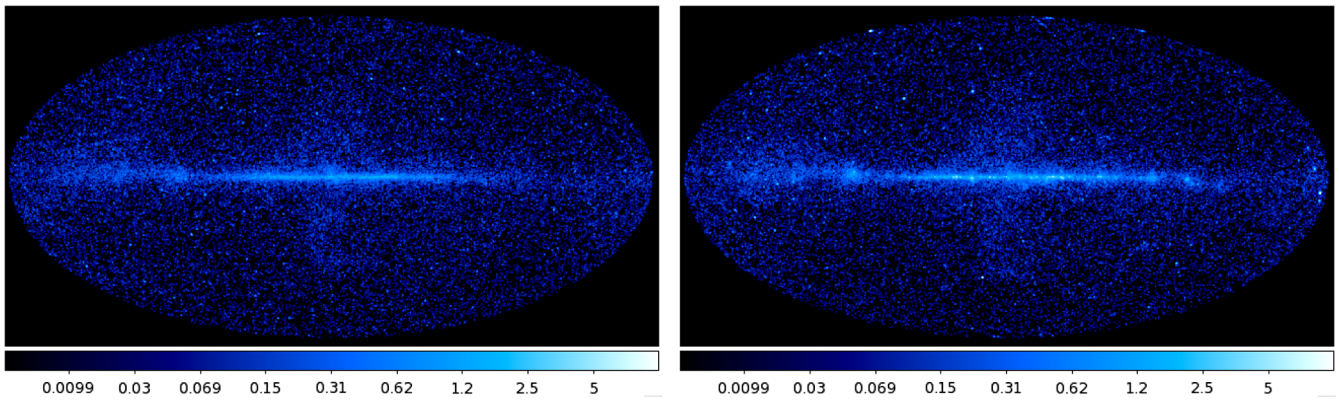

FIG. 1. In the left (right) panel the adaptively smoothed count map of one simulation (real sky) in the energy range 50 GeV–2 TeV is represented in Galactic coordinates and Hammer-Aitoff projection. The two maps contain about 60 000 γ-ray events.

performed an all-sky survey at > 50 GeV, resulting in the detection of 360 γ-ray sources that constitute the second catalog of hard Fermi-LAT sources (2FHL) [8].

Blazars, mostly belonging to the BL Lacertae (BL Lac) population, are the majority (74%) of the sources in the 2FHL catalog. At Galactic latitudes (b) larger than 10° about 70% of the detected sources are associated with BL Lacs. Only 7% of these high-latitude ($|b| > 10°$) sources are classified as something other than BL Lacs, 4% of which as Flat Spectrum Radio Quasars (FSRQs) and 3% as Radio Galaxies. Blazars of uncertain type and unassociated sources constitute the remaining 23% of the sample. The median of the synchrotron peak frequencies for blazars of uncertain type is very similar to that of BL Lacs [$\log_{10}(\nu^S_{\rm peak}/{\rm Hz}) = 15.7$ vs 15.6]. The same holds for the median spectral index of unassociated sources ($\Gamma = 3.0$ vs 3.1). This is supporting the fact that blazars of uncertain type and unassociated sources are almost entirely BL Lacs. Therefore, the fraction of likely blazars in the high-latitude 2FHL sample is 97% (93% BL Lacs and 4% FSRQs).

In this Letter, we derive the source detection efficiency of the 2FHL catalog analysis using accurate Monte Carlo simulations of the γ-ray sky. We then infer the intrinsic flux distribution dN/dS of sources located at a latitude $|b| > 10°$, where S is the photon flux (ph cm^{-2} s^{-1}) measured in the 50 GeV–2 TeV energy band.

The simulations were performed using the gtobssim tool, which is part of the Fermi ScienceTools distribution, and using the same pointing and live time history and event selection as used in the 2FHL catalog. We have employed the P8R2_SOURCE_V6 instrument response function for the simulations and analysis and the Galactic and isotropic diffuse emission were simulated using the GLL_IEM_V06.FITS and ISO_P8R2_SOURCE_V6_V06.TXT templates; see Ref. [9]. The last ingredient of the simulations is an isotropic population of point sources that has the characteristics of blazars (fluxes and spectra) as detected in 2FHL. The simulations described here were produced iteratively and ultimately rely on the source count distribution $dN/dS \propto S^{-\alpha}$ as determined at the end of photon fluctuation analysis (see later), which is a broken power law with a break flux $S_b = 1 \times 10^{-11}$ ph cm^{-2} s^{-1} and a Euclidean slope above the break, $\alpha_1 = 5/2$, while below S_b the slope is $\alpha_2 = 1.65$. Sources were generated with fluxes in the range $[S_{\rm min}, S_{\rm max}] = [10^{-14}, 10^{-9}]$ ph cm^{-2} s^{-1} and with power-law spectra of the form $dN/dE \propto E^{-\Gamma}$. For each source the photon index Γ is drawn from a Gaussian distribution with average value 3.2 and standard deviation 0.7 (this reproduces the observed distribution as shown on the bottom panel of Fig. 2). Galactic sources are not considered in the simulations since we are interested in the flux distribution of blazars at $|b| > 10°$. We produced 10 simulations of the γ-ray sky following these prescriptions and in Fig. 1 the sky map of one simulation is shown together with the real one. Clearly visible in both maps are the diffuse emission along the Galactic plane, the Fermi bubbles [10], the emission from point sources and the isotropic diffuse emission.

The energy spectrum of the simulations is consistent within 10%, at all energies of interest and for photons detected at $|b| > 10°$, with that of the LAT observations. As clearly visible in Fig. 1, the spatial distribution of gamma rays of the real map is also correctly reproduced. The 10 simulations are analyzed exactly as the real data were for the 2FHL catalog. This starts from detecting source candidates using a sliding-cell algorithm and a wavelet analysis [11] then analyzing each with the standard Fermi ScienceTools, in order to derive the γ-ray properties of detectable sources (see Ref. [8] for more details). As in the 2FHL catalog, detected sources are those with a test statistic $(TS) > 25$ and at least 3 associated photons predicted by the likelihood fit. This leads to the detection, in the simulations, of 271 ± 18 sources at $|b| > 10°$, which is in good agreement with the 253 sources detected in the 2FHL. Moreover, the simulations show that the 2FHL catalog contains at most 1% of false detections.

In order to further validate our analysis we have performed two consistency checks on the simulations.

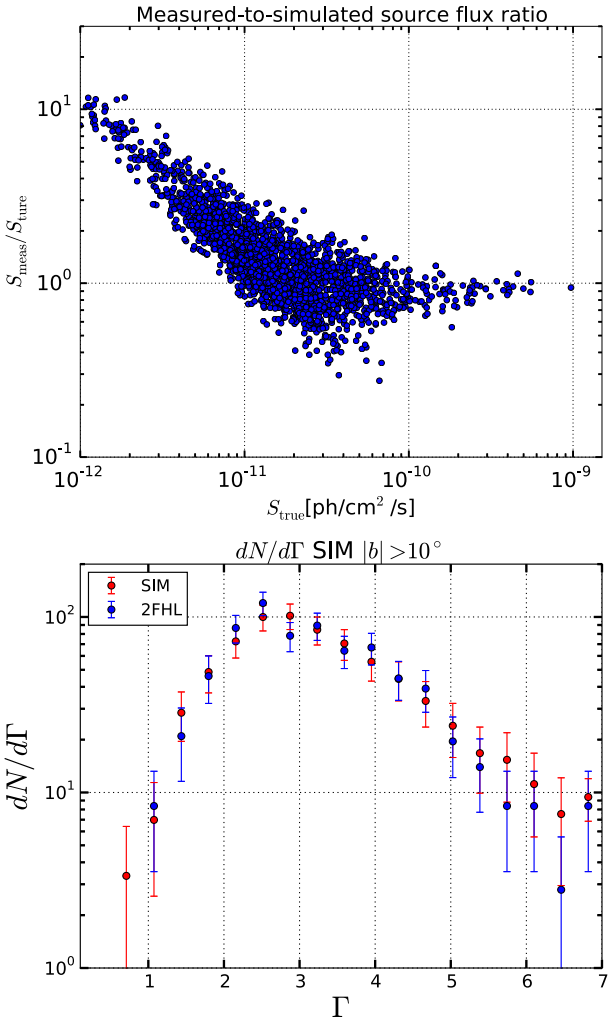

FIG. 2. Top panel: Ratio of the measured-to-simulated source flux (as derived from the analysis of the simulations described in the text) as a function of simulated source flux. Bottom panel: Comparison between the photon index distributions of sources detected in 2FHL (blue points) and the average of the simulations (red points).

The first compares the input source fluxes $S_{\rm true}$ with the fluxes $S_{\rm meas}$ measured with the Fermi Science Tools in the simulations. The result displayed in the top panel of Fig. 2 shows that for bright sources this ratio converges to 1 as expected in the absence of biases or errors. On the other hand, $S_{\rm meas}/S_{\rm true}$ for faint sources deviates systematically from 1. This effect is readily understood as caused by the Eddington bias, which is the statistical fluctuations of sources with a simulated flux below the threshold to a flux above the detection threshold [12]. Our second check compares the average photon index distribution ($dN/d\Gamma$), as derived from the simulations, with the same distribution as derived from the 2FHL catalog. This is reported in the bottom panel of Fig. 2 and it shows that our description of the γ-ray sky and of the blazar population is faithful to the real one.

The results from analyzing the sources in the simulated data can be used to measure the detection efficiency $\omega(S)$, which is a weighting factor that takes into account the probability to detect a source as a function of flux. The detection efficiency is simply derived from the simulations, measuring the ratio between the number of detected sources and the number of simulated ones as a function of measured source flux. The result reported in Fig. 3 shows that the LAT detects any source in the $|b| > 10°$ sky for fluxes

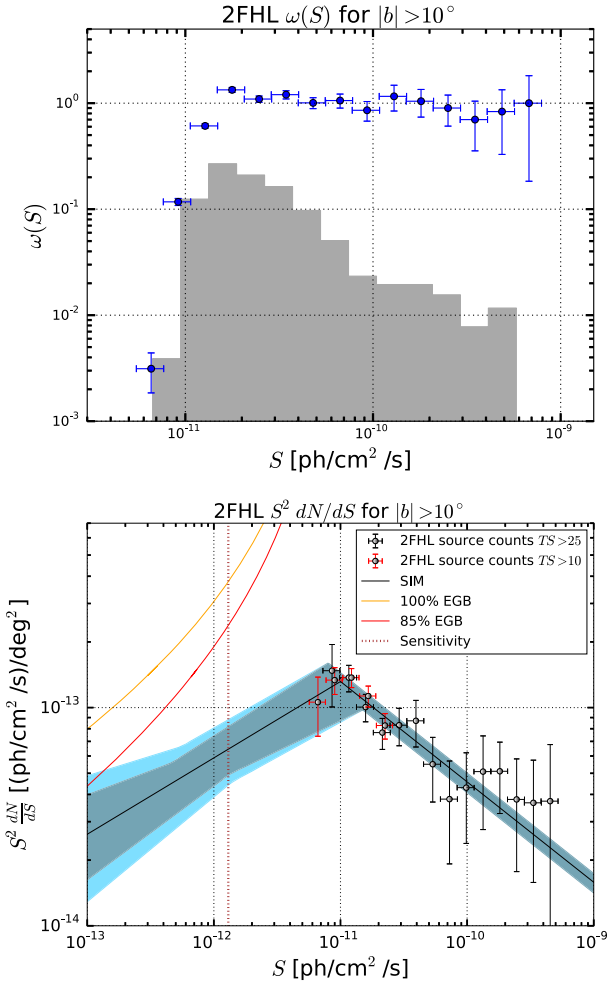

FIG. 3. Top panel: Detection efficiency $\omega(S)$ (blue points) as a function of source flux and normalized distribution of source fluxes detected in 2FHL (gray shaded histogram). Bottom panel: Intrinsic S^2dN/dS distribution measured with two different cuts on the source TS: 25 (black points) and 10 (red points, for the lowest four flux bins only). The black solid line shows our best-fit model, while the gray and cyan bands show the 1σ and 3σ uncertainty bands from the photon fluctuation analysis. The vertical brown dotted line represents the sensitivity of the photon fluctuation analysis. The orange and red curves indicate where 85% and 100% of the EGB intensity above 50 GeV [2]. Taking the 100% curve as an example, any point on that curve that is joined with a power law to the measured source count distribution at $S \approx 10^{-11}$ ph cm^{-2} s^{-1}, will give a source count distribution that produces 100% of the EGB.

larger than $\approx 2 \times 10^{-11}$ ph cm^{-2} s^{-1}, but misses 80%–90% of the sources with fluxes of $\approx 1 \times 10^{-11}$ ph cm^{-2} s^{-1} and many more below this flux. The peak $[\omega(S) > 1]$ clearly visible at a flux of $\approx 2 \times 10^{-11}$ ph cm^{-2} s^{-1} is due to the Eddington bias. We have verified that our estimate of the detection efficiency is insensitive to the choice of break flux by repeating the analysis with breaks occurring at fluxes as low as $S_b \geq 5 \times 10^{-12}$ ph cm^{-2} s^{-1}, i.e., well below the fitted range determined from the photon fluctuation analysis described later.

A reliable estimate of the detection efficiency is fundamental in order to correct the observed flux distribution of the 2FHL catalog and in turn to derive the intrinsic source count distribution, which is obtained as

$$\frac{dN}{dS}(S_i) = \frac{1}{\Omega \Delta S_i} \frac{N_i}{\omega(S_i)} \qquad [\text{cm}^2\,\text{s}\,\text{deg}^{-2}], \qquad (1)$$

where Ω is the solid angle of the $|b| > 10°$ sky, ΔS_i is the width of the flux bin, N_i is the number of sources in each flux bin, and S_i is the flux at the center of a given bin i. We verified through simulations that this method allows us to retrieve the correct source count distribution as long as the distribution used in the simulations is a faithful representation of the real one.

This is found to be consistent, down to the sensitivity of the 2FHL catalog ($\approx 8 \times 10^{-12}$ ph cm^{-2} s^{-1}), with a power-law function with slope $\alpha_1 = 2.49 \pm 0.12$ (see bottom panel of Fig. 3). This best-fit value is consistent with the Euclidean expectation and motivated us to choose $\alpha_1 = 2.5$ in the simulations.

Figure 4 shows the cumulative source count distribution that is defined as

$$N(>S) = \int_S^{S_{\max}} \frac{dN}{dS'} dS' \qquad [\text{deg}^{-2}], \qquad (2)$$

where $S_{\max}$ is fixed to be 10^{-8} ph cm^{-2} s^{-1}.

In order to infer the shape of the dN/dS distribution below the flux threshold for detecting point sources we have performed a photon fluctuation analysis. This helps us to probe the source count distribution to the level where sources contribute on average 0.5 photons each. The photon fluctuation analysis has been successfully used in the past to predict the shape of dN/dS below the sensitivity of ROSAT [17] before Chandra and XMM, about one decade later, detected those faint sources [18]. The analysis is performed by comparing the histogram of the pixel counts of the real sky with the ones obtained via Monte Carlo simulations and allows us to constrain the slope of the differential flux distribution below the threshold of the survey [17,19]. We consider a differential flux distribution described as a broken power law where the slope above the break is $\alpha_1 = 2.5$ as determined in this work while below the break the slope varies in different

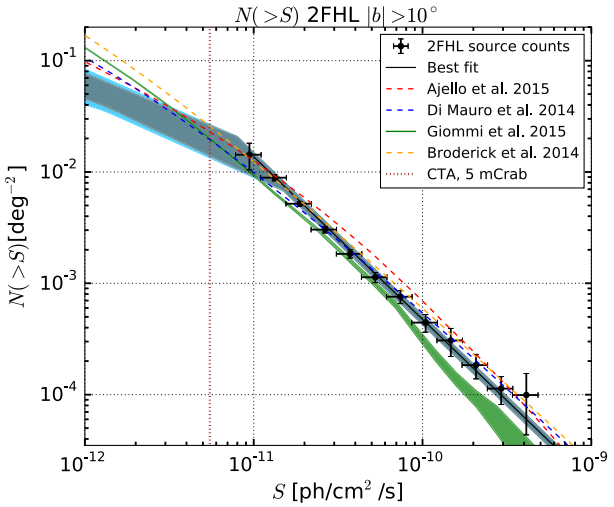

FIG. 4. Cumulative source count distribution $N(>S)$ with the uncertainty bands as in Fig. 3 together with the theoretical predictions from Refs. [13] (blue dashed line), [4] (red dashed line), [14] (green band), and [15] (orange dashed line). The vertical dotted brown line shows the 5 mCrab flux reachable by CTA in 240 h of exposure [16].

simulations between $\alpha_2 \in [1.3, 2.7]$. For each value of the slope we derive the model pixel count distribution averaging over the pixel count distributions obtained from 20 simulations. The simulated and real maps have been pixelized using the HEALPix tool [20] [21]. We have used a resolution of order 9, which translates into 314 572 8 pixels and a pixel size of about 0.11°. Consistent results are obtained when using a resolution of order 8. We consider a single energy bin from 50 GeV to 2 TeV.

The model (averaged) pixel count distributions are compared to the real data using a χ^2 analysis to determine the most likely scenario. As expected, there is a degeneracy between the best-fit value of the slope α_2 and the choice of the break flux, S_b. The result of the analysis is that the break flux is limited to the range between $S_b \in [8 \times 10^{-12}, 1.5 \times 10^{-11}]$ ph cm^{-2} s^{-1} while the index below the break is in the range $\alpha_2 \in [1.60, 1.75]$. The best configuration, which we refer to as our benchmark model, has a break flux at 1×10^{-11} ph cm^{-2} s^{-1} and a slope $\alpha_2 = 1.65$ with a $\chi^2 = 12.4$ (for 12 degrees of freedom). This implies that the source count distribution must display a hard break $|\alpha_1 - \alpha_2| \approx 0.9$ from the Euclidean behavior measured at bright fluxes. We show in Fig. 5, for the best-fit configuration, the comparison between the pixel count distribution evaluated for the average of 20 simulations, and the same quantity as derived from the real data. The figure also shows the differences between these two distributions.

The presence of a break at about 1×10^{-11} ph cm^{-2} s^{-1} is corroborated by the number of detected sources, that for our benchmark source count distribution is found to be consistent with the 2FHL (271 ± 18 vs 253 in the 2FHL). As soon as we move the position of the break to lower

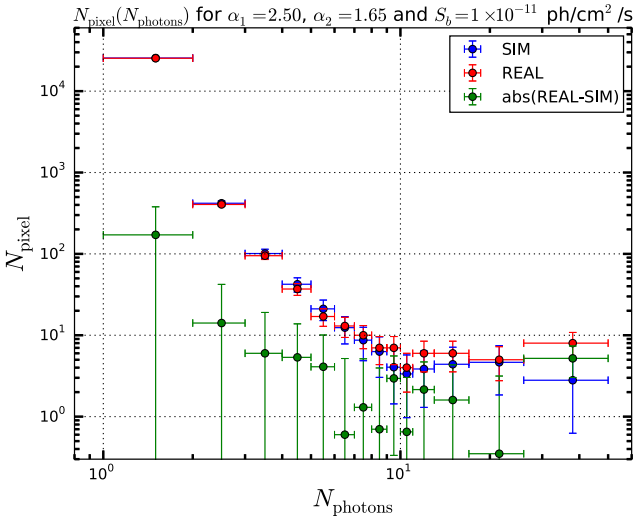

FIG. 5. Comparison between the pixel count distribution from the average of 20 simulations (blue points), and the distribution from the real sky (red points). The green points show the difference between the two distributions. In each number of photon bin $N_{\rm photons}$ ranging between $[N_{\rm photon,1}, N_{\rm photon,2}]$, we display $N_{\rm pixel}$ with $N_{\rm photons} \in [N_{\rm photon,1}, N_{\rm photon,2})$.

fluxes, the expected number of detected sources becomes quickly incompatible with the values measured in the 2FHL, even when compensating by making α_2 steeper (e.g., for $S_b = 5 \times 10^{-12}$ ph cm^{-2} s^{-1} and $\alpha_2 = 1.10$, we predict 318 ± 20 sources).

Alternatively, it is possible to probe directly flux values below the 2FHL detection threshold by applying a source TS cut lower than the nominal value of 25 used for the construction of the catalog. As long as the source detection efficiency is self-consistently derived, the intrinsic source count distribution is independent of the TS cut and lower cut values translate into lower detection thresholds. By repeating the analysis with $TS > 10$ we were able to add a new point at about 6×10^{-12} ph cm^{-2} s^{-1} that, albeit with a relatively large error, corroborates the presence of a break at 1×10^{-11} ph cm^{-2} s^{-1} (see bottom panel of Fig. 3).

Finally, we have checked that the shape of the derived dN/dS distribution is not significantly affected by a change of α_1 within its error.

The lowest flux that the photon fluctuation analysis is sensitive to can be estimated by adding to the source count distribution one more break flux below that of the benchmark model. We fixed the slope below this second break to $\alpha_3 = 1.80$, which is at the edge of the derived range for α_2, while the break flux is varied in the range $S_{\rm lim} \in [5 \times 10^{-13}, 5 \times 10^{-12}]$ ph cm^{-2} s^{-1} to register when a worsening of the χ^2 (with respect to the best-fit one) is observed. The result of this analysis is that the fit worsened by more than 3σ for $S_{\rm lim} \gtrsim 1.3 \times 10^{-12}$ ph cm^{-2} s^{-1}. The results of the photon fluctuation analysis are reported in Figs. 3 and 4, which show that this technique allows us to measure the source count distribution over almost three decades in flux.

In the bottom panel of Fig. 3, we show the fluxes at which a source count distribution with any given slope α_2 below $S_b = 1 \times 10^{-11}$ ph cm^{-2} s^{-1} would produce 100% (or 85%) of the EGB.

We have tested also the possibility that a new s ource population could emerge in the flux distribution with a Euclidean distribution, as might be expected, for example, from star-forming galaxies [22]. In this test we set $\alpha_3 = 2.50$ and follow the method described above to derive the maximum flux at which a possible resteepening of the source counts might occur. This is found to be $S_{\rm lim} \approx 7 \times 10^{-13}$ ph cm^{-2} s^{-1} and the integrated emission of such a population would exceed at fluxes of $\sim 7 \times 10^{-14}$ ph cm^{-2} s^{-1}, the totality of the EGB intensity.

Our best-fit model for the flux distribution dN/dS is, therefore, for $S \gtrsim 10^{-12}$ ph cm^{-2} s^{-1}, a broken power-law with break flux in the range $S_b \in [0.8, 1.5] \times 10^{-11}$, slopes above and below the break of $\alpha_1 = 2.49 \pm 0.12$ and $\alpha_2 \in [1.60, 1.75]$, respectively, and a normalization $K = (4.60 \pm 0.35) \times 10^{-19}$ deg^{-2} ph^{-1} cm^2 s. We believe this describes the source counts of a single population (blazars), because no resteepening of the source count distribution is observed and because the large majority (97%) of the detected sources are likely blazars.

Figure 4 reports the theoretical expectations for the source count distribution given by blazars [4,14] and BL Lacs [13]. These models are consistent with the observations at bright fluxes, but are above the experimental $N(>S)$ by about a factor of 2 at $S = 10^{-12}$ ph cm^{-2} s^{-1}. We include in the same figure also the predicted 5 mCrab sensitivity reachable by CTA in 240 h in the most sensitive pointing strategy [16]. At these fluxes the source density is 0.0194 ± 0.0044 deg^{-2}, which translates to the serendipitous detection of 200 ± 45 blazars in one quarter of the full sky. It is also interesting to note that our analysis constrains the source count distribution to fluxes that are much fainter than those reachable by CTA in short exposures.

Once known, the source count distribution can be used to estimate the contribution of point sources to the EGB. This is performed by integrating the flux distribution dN/dS as follows:

$$I = \int_0^{S_{\rm max}} S' \frac{dN}{dS'} dS' \qquad [\text{ph cm}^{-2}\,\text{s}^{-1}\,\text{sr}^{-1}]. \qquad (3)$$

Choosing $S_{\rm max} = 10^{-8}$ ph cm^{-2} s^{-1} we find that the total integrated flux from point sources is $2.07^{+0.40}_{-0.34} \times 10^{-9}$ ph cm^{-2} s^{-1} sr^{-1}, which constitutes 86^{+16}_{-14}% (The quoted range takes into account only the uncertainty on the photon fluctuation analysis and can extend above 100%. Indeed, it does not consider possible systematic correlations between the cumulative intensity of sources and the intensity of the EGB, which were measured in two separate analyses.) of the EGB above 50 GeV estimated in Ref. [2]. This validates the predictions of models [4,5,13].

This calculation contains an extrapolation of the derived source count distribution below the sensitivity of the pixel counting. Point sources with fluxes $S > 1.3 \times 10^{-12}\,\mathrm{ph\,cm^{-2}\,s^{-1}}$ produce $1.47^{+0.20}_{-0.24} \times 10^{-9}\,\mathrm{ph\,cm^{-2}\,s^{-1}\,sr^{-1}}$ (61% of the EGB), while $6.0^{+2.0}_{-1.0} \times 10^{-10}\,\mathrm{ph\,cm^{-2}\,s^{-1}\,sr^{-1}}$ (25% of the EGB) is produced by sources below that flux.

The Fermi LAT has measured the angular power spectrum of the diffuse γ-ray background at $|b| > 30°$ and in four energy bins spanning the 1–50 GeV energy range [23]. For multipoles $l \geq 155$ the angular power C_P is found to be almost constant, suggesting that the anisotropy is produced by an unclustered population of unresolved point sources. Indeed, Refs. [24–26] argue that most of the angular power measured by the Fermi LAT is due to unresolved emission of radio-loud active galactic nuclei.

The angular power due to unresolved sources at > 50 GeV can be readily predicted from the source count distribution as

$$C_P = \int_0^{S_{\mathrm{max}}} [1 - \omega(S')] S'^2 \frac{dN}{dS'} dS' [\mathrm{sr^{-1}}]. \qquad (4)$$

The angular power evaluates to $C_P(E > 50\ \mathrm{GeV}) = 9.4^{+1.0}_{-1.6} \times 10^{-22}\ (\mathrm{ph/cm^2/s})^2\,\mathrm{sr^{-1}}$. This is the first observationally based prediction of the angular power at > 50 GeV. Our estimation for $C_P(E > 50\ \mathrm{GeV})$ is in good agreement with the extrapolation of the Fermi-LAT angular power measurements [23] above 50 GeV and is consistent with the calculated anisotropy due to radio loud active galactic nuclei made in Refs. [24,25].

In conclusion, the Fermi-LAT Collaboration has used the new event-level analysis Pass 8 to conduct an all-sky survey above 50 GeV. The resulting 2FHL catalog contains 253 sources at $|b| > 10°$ and closes the energy gap between the LAT and Cherenkov telescopes. We have thoroughly studied the properties of both resolved and unresolved sources in the 50 GeV–2 TeV band using detailed Monte Carlo simulations and a photon fluctuation analysis. This allowed us to characterize, for the first time, the source count distribution above 50 GeV, which is found to be compatible at $\gtrsim 10^{-12}\ \mathrm{ph\,cm^{-2}\,s^{-1}}$ with a broken power-law model with a break flux in the range $S_b \in [0.8, 1.5] \times 10^{-11}\ \mathrm{ph\,cm^{-2}\,s^{-1}}$, and slopes above and below the break of, respectively, $\alpha_1 = 2.49 \pm 0.12$ and $\alpha_2 \in [1.60, 1.75]$. A photon fluctuation analysis constrains a possible resteepening of the flux distribution to a Euclidean behavior ($\alpha_3 = 2.50$) to occur at fluxes lower than $\sim 7 \times 10^{-13}\ \mathrm{ph\,cm^{-2}\,s^{-1}}$. Our analysis permits us to estimate that point sources, and, in particular, blazars, explain almost the totality ($86^{+16}_{-14}\%$) of the > 50 GeV EGB.

This might have a number of important consequences, since any other contribution, exotic or not, must necessarily be small. This bound might imply strong constraints for the annihilation cross section or decay time of high-mass dark matter particles producing γ rays [4,5]. Tight constraints could also be inferred on other γ-ray emission mechanisms due to other diffusive processes such as UHECRs [27,28]. Finally, if the neutrinos detected by IceCube have been generated in hadronic cosmic-ray interactions, then the same sources producing the neutrino background will produce part of the sub-TeV γ-ray background [29]. Because blazars were found not to be responsible for the majority of the neutrino flux [30], the fact that the 50 GeV–2 TeV γ-ray background is almost all due to blazars constrains the contribution of other source classes to the neutrino background. Such constraints will be presented in a dedicated paper.

The Fermi-LAT Collaboration acknowledges support for LAT development, operation, and data analysis from NASA and DOE (United States), CEA/Irfu and IN2P3/CNRS (France), ASI and INFN (Italy), MEXT, KEK, and JAXA (Japan), and the K. A. Wallenberg Foundation, the Swedish Research Council, and the National Space Board (Sweden). Science analysis support in the operations phase from INAF (Italy) and CNES (France) is also gratefully acknowledged.

*majello@slac.stanford.edu
†mattia.dimauro@to.infn.it

[1] C. E. Fichtel, R. C. Hartman, D. A. Kniffen, D. J. Thompson, H. Ogelman, M. E. Ozel, T. Tumer, and G. F. Bignami, Astrophys. J. **198**, 163 (1975).
[2] M. Ackermann *et al.* (Fermi-LAT Collaboration), Astrophys. J. **799**, 86 (2015).
[3] C. D. Dermer, Astrophys. J. **659**, 958 (2007).
[4] M. Ajello, D. Gasparrini, M. Sánchez-Conde, G. Zaharijas, M. Gustafsson *et al.*, Astrophys. J. **800**, L27 (2015).
[5] M. Di Mauro and F. Donato, Phys. Rev. D **91**, 123001 (2015).
[6] M. Fornasa and M. A. Sánchez-Conde, arXiv:1502.02866.
[7] W. Atwood, L. Baldini, J. Bregeon, P. Bruel, A. Chekhtman *et al.*, Astrophys. J. **774**, 76 (2013).
[8] Fermi-LAT Collaboration, arXiv:1508.04449.
[9] http://fermi.gsfc.nasa.gov/ssc/.
[10] M. Ackermann *et al.* (Fermi-LAT Collaboration), Astrophys. J. **793**, 64 (2014).
[11] S. Ciprini, G. Tosti, F. Marcucci, C. Cecchi, G. Discepoli, E. Bonamente, S. Germani, D. Impiombato, P. Lubrano, and M. Pepe, in *The First GLAST Symposium*, edited by S. Ritz, P. Michelson, and C. A. Meegan, *AIP Conf. Proc.* 921, 546 (2007).
[12] A. S. Eddington, Mon. Not. R. Astron. Soc. **73**, 359 (1913).
[13] M. Di Mauro, F. Donato, G. Lamanna, D. Sanchez, and P. Serpico, Astrophys. J. **786**, 129 (2014).
[14] P. Giommi and P. Padovani, Mon. Not. R. Astron. Soc. **450**, 2404 (2015).
[15] A. E. Broderick, C. Pfrommer, E. Puchwein, and P. Chang, Astrophys. J. **790**, 137 (2014).

[16] G. Dubus, J. L. Contreras, S. Funk, Y. Gallant, T. Hassan, J. Hinton, Y. Inoue, J. Knödlseder, P. Martin, N. Mirabal *et al.*, Astropart. Phys. **43**, 317 (2013).
[17] G. Hasinger, R. Burg, R. Giacconi, G. Hartner, M. Schmidt, J. Trumper, and G. Zamorani, Astron. Astrophys. **275**, 1 (1993).
[18] R. Gilli, A. Comastri, and G. Hasinger, Astron. Astrophys. **463**, 79 (2007).
[19] D. Malyshev and D. W. Hogg, Astrophys. J. **738**, 181 (2011).
[20] http://healpix.sourceforge.net/.
[21] K. M. Górski, E. Hivon, A. J. Banday, B. D. Wandelt, F. K. Hansen, M. Reinecke, and M. Bartelmann, Astrophys. J. **622**, 759 (2005).
[22] M. Béthermin, E. Daddi, G. Magdis, M. T. Sargent, Y. Hezaveh, D. Elbaz, D. Le Borgne, J. Mullaney, M. Pannella, V. Buat *et al.*, Astrophys. J. Lett. **757**, L23 (2012).
[23] M. Ackermann, M. Ajello, A. Albert *et al.*, Phys. Rev. D **85**, 083007 (2012).
[24] A. Cuoco, E. Komatsu, and J. Siegal-Gaskins, Phys. Rev. D **86**, 063004 (2012).
[25] M. Di Mauro, A. Cuoco, F. Donato, and J. M. Siegal-Gaskins, J. Cosmol. Astropart. Phys. 11 (2014) 021.
[26] A. E. Broderick, C. Pfrommer, E. Puchwein, K. M. Smith, and P. Chang (Heidelberg Institute for Theoretical Studies, Perimeter Institute for Theoretical Physics), Astrophys. J. **796**, 12 (2014).
[27] M. Ahlers and J. Salvado, Phys. Rev. D **84**, 085019 (2011).
[28] G. B. Gelmini, O. Kalashev, and D. V. Semikoz, J. Cosmol. Astropart. Phys. 01 (2012) 044.
[29] M. Aartsen *et al.* (IceCube Collaboration), Phys. Rev. Lett. **113**, 101101 (2014).
[30] T. Glüsenkamp *et al.* (IceCube Collaboration), arXiv:1502.03104.